Article

Material Flow and Microstructural Evolution in Friction Stir Welding of LAZ931 Duplex Mg-Li Alloys

Shiquan Cui [1], **Wenguan Cao** [1], **Qi Zhang** [1], **Liguo Wang** [1,2], **Yufeng Sun** [1,2,*] and **Shaokang Guan** [1,2]

[1] School of Materials Science and Engineering, Zhengzhou University, Zhengzhou 450001, China; sqcui@hotmail.com (S.C.); caoweng@hotmail.com (W.C.); zq769598@outlook.com (Q.Z.); lgwang@zzu.edu.cn (L.W.); skguan@zzu.edu.cn (S.G.)
[2] Henan Province Key Laboratory of Advanced Light Alloys, Zhengzhou University, Zhengzhou 450001, China
* Correspondence: yfsun@zzu.edu.cn

Abstract: The material flow behavior during friction stir welding (FSW) plays a critical role in the quality of final joints. In this study, the FSW of LAZ931 duplex Mg alloy was carried out at a rotation speed of 800 rpm and welding speeds of 50, 100, and 200 mm/min, respectively. A thin pure Mg strip inserted at the interface between the two Mg-Li alloy plates was used as a marker to study the flow behavior of the materials in the FSW process. Sound welds with no defects were obtained for all three welding speeds. The microstructural evaluations along the marker on the horizontal cross-section around the keyhole of the welds were characterized. As the welding speed increased, the marker came closer to the keyhole, indicating the decreased extent of the plastic deformation of the material. In the shoulder-affected zone (SAZ), the thickness of the marker reduced gradually in the accelerating stage and finally accumulated together in the decelerating stage. However, in the pin-affected zone (PAZ), the thickness of the marker reduced sharply in the accelerating stage and then became dispersed in the decelerating stage, and the degree of dispersion decreased as the weld speed increased. As a result, an elongated grain structure was formed in the SAZ, while two equiaxial grain structures were formed in the PAZ. The material on the advancing side was refined by the pin and deposited in the weld to form a fine equiaxial grain structure due to the high strain rate. In contrast, the material on the retreating side was pushed by the pin and thus directly deposited in the weld to form a coarse equiaxial grain structure. In addition, the area of the fine equiaxial grain structure was reduced obviously with the increase in welding speed.

Keywords: friction stir welding; material flow; Mg-Li alloy; microstructure

1. Introduction

Mg-Li alloy is currently the lightest structural metallic material and has a great potential to be widely used in aerospace, automobile manufacturing, and military protection due to its high specific strength, high specific stiffness, and excellent shock and impact resistance [1–3]. However, when Mg-Li alloys are subjected to conventional fusion welding, sound welds are difficult to obtain and defects are prone to be generated due to the presence of chemically active Li elements. In addition, excessive high temperature could cause burning, grain coarsening, and other solidification defects of the Mg-Li alloys, which significantly deteriorates the mechanical properties of the joints [4–7].

Friction stir welding (FSW) is a solid-state welding technology invented by TWI in 1991. During FSW, a high-speed rotating tool is penetrated into the faying surfaces of the workpieces to be welded, bringing the material to a viscoplastic state and forming a defect-free weld with the traveling of the tool [8–10]. Since the welding temperature during the entire FSW process is far below the melting point of the materials to be welded, the problem accompanied with the fusional welding technology might be successfully avoided. For example, Liu and Xu et al. successfully performed the FSW of Mg-Li alloys

and defect-free joints were obtained [11,12]. Tsujikawa et al. [13] conducted the FSW of cold-rolled LA141 Mg-Li alloys and showed that sound joints could be formed under various conditions. Zhou et al. [14] carried out the FSW of 3 mm thick LZ91 Mg-Li alloy and obtained a joint with strength exceeding that of the base metal (BM). Gao et al. [15] also obtained a 3 mm thick LAZ933 Mg-Li alloy FSW joint and found that the α-phase dissolved in the stir zone (SZ) with a refined grain structure. The joint strength was higher than that of the BM due to the precipitation-strengthening effect. However, the friction-stir-welded Mg-Li alloy joints usually showed an obvious fine grain structure in the advancing side (AS) and a remarkable coarse grain structure in the retreating side (RS) within the SZ. Zhou et al. [16] showed that such a microstructural difference in the FSW Mg-Li alloy joints could be alleviated after reciprocal FSW. However, the mechanism underlying the significant difference in the microstructure within the SZ remains unclear. Furthermore, most of the current studies on the FSW of Mg alloys focuses on single-phase alloy, with comparably fewer studies examining the dual-phase Mg-Li alloy FSW.

It is well known that FSW is a complex process involving material flow and plastic deformation at an elevated temperature, which are crucial in determining the formation of the final weld. A comprehensive understanding of the plastic material flow behavior and microstructural evolution during FSW is essential for elucidating the weld formation mechanism and optimizing the welding process [17,18]. However, the material flow caused by the rotating tool is very complex and the formation of the weld seam takes place in a confined space, which is difficult to observe directly. To solve this problem, studies have been extensively carried out on the visualization of the material flow. The methods used so far mainly include the marker material method, X-ray radiography, and numerical simulation [19–22].

In 1999, Collgan [23] first introduced the tracing method using steel balls to study the material flow in the FSW processes of Al alloys, demonstrating that the material flow involves a mixture of mixing and squeezing. By observing the distribution of the tracer material, the actual flow path of the materials could be intuitively verified. During the welding process, various microstructures can be obtained depending on the different material flow behaviors. Zhang et al. [24] showed that the material flow during the FSW of Mg alloys came from two main sources, one from the AS and the other from the RS, and the material flow on the AS determined whether or not the weld defects could be formed. Liu et al. [25] assessed the strain and strain rate in the FSW of pure Cu by measuring the dimensional changes in the CuZn alloy marker. The material flow around the probe could be divided into five stages. A pronounced strain reversal was observed in the shoulder-affected zone (SAZ) but not in the pin-affected zone (PAZ). It was recently found that the strain and strain rate of the material flow on the AS and RS were remarkably different during FSW, which led to the different microstructure within the SZ of the final weld [25,26]. Typically, the microstructure near the AS exhibits a more distinct demarcation from the base metal (BM) compared to the RS due to the higher strain rate in the AS.

The LAZ931 (Mg-Li9-Al3-Zn1) dual-phase Mg-Li alloy contains a hexagonal close-packed (HCP) α-Mg phase and a body-centered cubic (BCC) β-Li phase. During the FSW of LAZ931 alloy, a coarse grain structure and fine-grain structured region with an obvious boundary were formed within the SZ. The joints usually fractured along the boundary during tensile tests due to the incompatible plastic deformation between the different grain structures, which significantly deteriorated its mechanical properties [27].

In order to study the material flow during the FSW of duplex-phase Mg-Li alloys and to explore the effect of the welding parameters on the microstructural evolution of the joints, a 5.2 mm thick LAZ931 plate was subjected to FSW using a thin pure Mg strip as the marker. The flow trajectories of the pure Mg marker around the keyhole of the joints were examined and the microstructure of the Mg-Li alloys along the marker were characterized.

2. Materials and Methods

In this study, the hot-rolled LAZ931 Mg alloy plates with a dimension of $200 \times 50 \times 5.2$ mm^3 were subjected to the FSW process. Before the FSW, the Mg-Li alloy plates were mechanically polished to remove the oxide film on the surface, followed by cleaning with ethanol. The FSW was performed at a constant rotation speed of 800 rpm and varied welding speeds of 50 mm/min, 100 mm/min, and 200 mm/min under protective Ar gas. In order to study the material flow behavior during the FSW, a pure Mg strip with a thickness of 0.5 mm as a marker was inserted at the interface between the two LAZ931 plates manufactured in Zhengzhou Light Alloy Institute Co., Ltd., Zhengzhou, China. The chemical composition of the LAZ931 Mg alloy and the pure Mg strip are summarized in Table 1. A threaded rotating tool made of SKD61 steel was used during the FSW, which had a shoulder diameter of 15 mm, a pin length of 4.8 mm, a pin root diameter 6.9 mm, and a pin top diameter of 5.7 mm, respectively.

Table 1. Chemical composition of the LAZ931 Mg-Li alloy and pure Mg strip.

| Materials	Alloy Composition (wt.%)			
	Mg	**Li**	**Al**	**Zn**
Pure Mg	99.99	-		
LAZ931	86.7	8.9	3.5	0.9

After welding, microstructural evolutions along the pure Mg marker around the keyhole on horizontal planes 0.5 mm from the upper and lower surfaces of the joints were observed, respectively. For the optical microscope (OM) and scanning electron microscope (SEM) observation, the samples were mechanically polished to a mirror finish and then etched with a 4 wt.% nital solution. The schematic map of the FSW process and sampling positions for the microstructural characterization are shown in Figure 1.
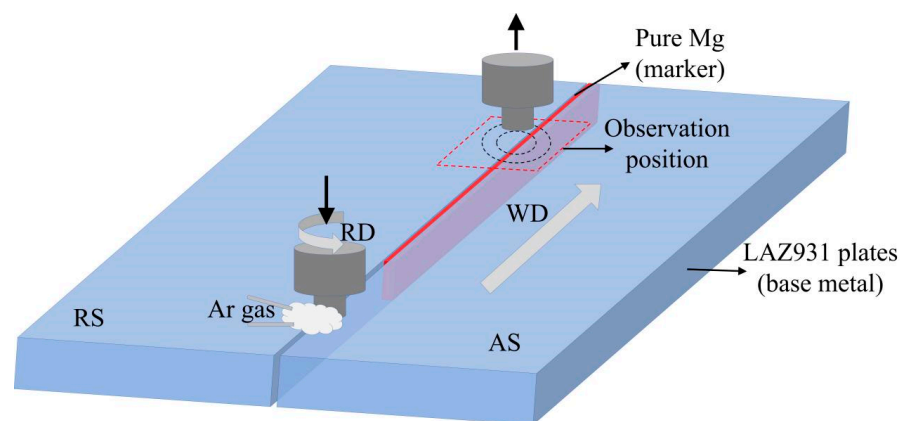
**Figure 1.** Schematic map of the FSW of LAZ931 alloy with the pure Mg marker.

3. Results and Discussion

The surface appearance of the FSW joints obtained at three different welding speeds were quite similar. As a typical example, Figure 2 shows the appearance of the FSW joint with a pure Mg marker between the two plates. The joint showed a smooth surface without any visible defects. A part of the pure Mg marker materials remained in front of the keyhole for later characterization.
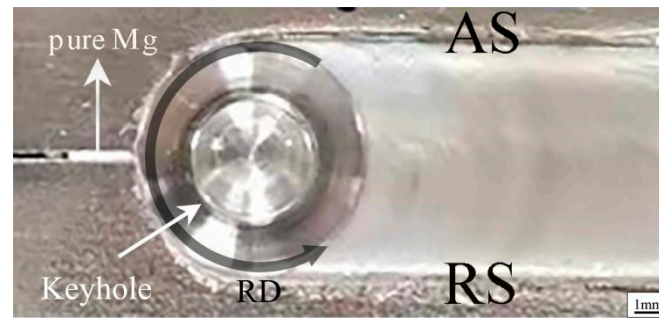
**Figure 2.** Appearances of the FSW joints (RD: rotation direction).

Figure 3 shows the cross-sectional macrostructure of the joints with marker materials obtained at different welding speeds, which was completely the same as those obtained at the same welding parameters without marker materials, as reported in Ref. [27]. The results indicate that the use of a pure Mg strip as a marker had no impact on the material flow during the FSW. Generally, the deformation behavior of the materials near the upper surface was mainly influenced by the tool shoulder, namely, the SAZ, while the deformation behavior of the materials in the lower part was mainly influenced by the tool pin, namely, the PAZ [25,28]. The SAZ and PAZ are distinguished according to the distinct characteristics of the marker material, as illustrated in the Figure 3. For the joints obtained at 50 mm/min, 100 mm/min, and 200 mm/min, the corresponding SAZ thicknesses were 1.34 mm, 1.41 mm, and 1.46 mm, respectively. In the PAZ, the white pure Mg marker divided the SZ into two parts due to the different grain structures. The fine grain structure was found near the AS and is therefore referred to as the fine-grained part (FGP), while near the RS coarse grain size was formed and is called the coarse-grained part (CGP). In addition, as the welding speed increased, the volume fraction of the FGP area in the PAZ decreased from 66.6% at 50 mm/min to 59.6% at 100 mm/min, and then to 57.6% at 200 mm/min.
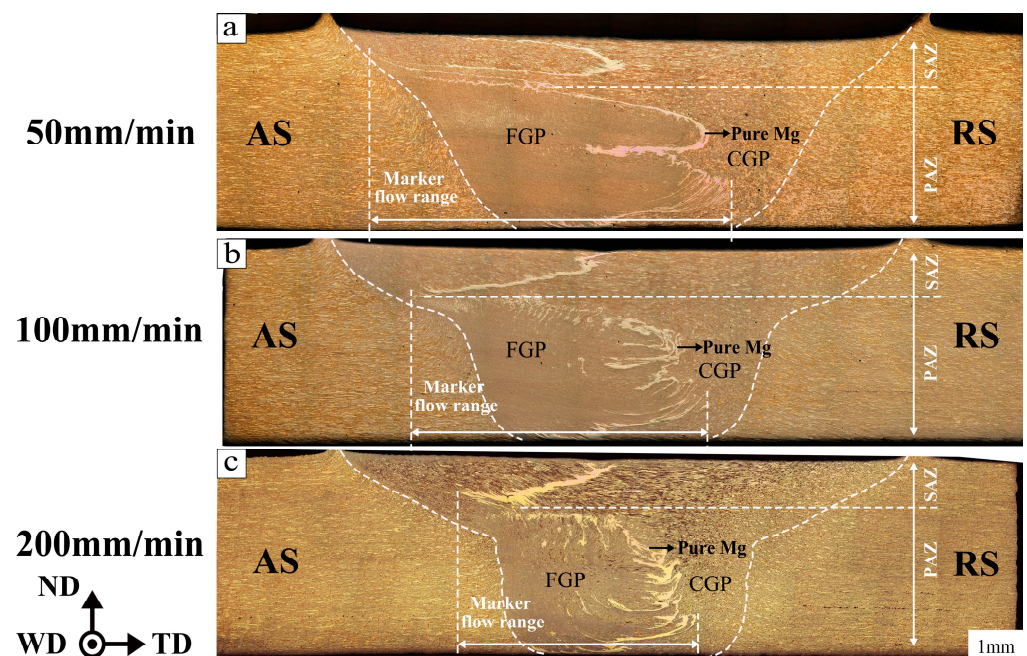
Figure 3. Cross-sectional macrostructure of the joints at different welding speeds. (**a**) 50 mm/min; (**b**) 100 mm/min; (**c**) 200 mm/min.

Figure 4 shows the higher magnification OM images of the BM, CGP, and FGP of the joint at 50 mm/min. Figure 4a shows the typical rolled microstructure of the BM, comprising the elongated α-Mg and β-Li phases, with black AlLi particles predominantly

distributed within the β-Li grains. In the SAZ, as shown in Figure 4b, the elongated grain structure of the BM was broken down into smaller sizes, yet the elongated grains persisted due to the horizontal shear stress by the shoulder. In the PAZ, the elongated grains in the BM were transformed into fine equiaxial grains due to the occurrence of dynamic recrystallization caused by the thermal and mechanical effects of the rotating tool. Figure 4c shows the microstructure of the FGP. The inserted image at a higher magnification confirmed the formation of fine α-Mg and β-Li phases. Figure 4d shows the microstructure of the CGP, where α-Mg had aggregated into large clumps as a result of dynamic grain growth (DGG) [27]. Notably, the number of AlLi particles was drastically reduced compared to those in the BM due to the solid solution at high temperatures.
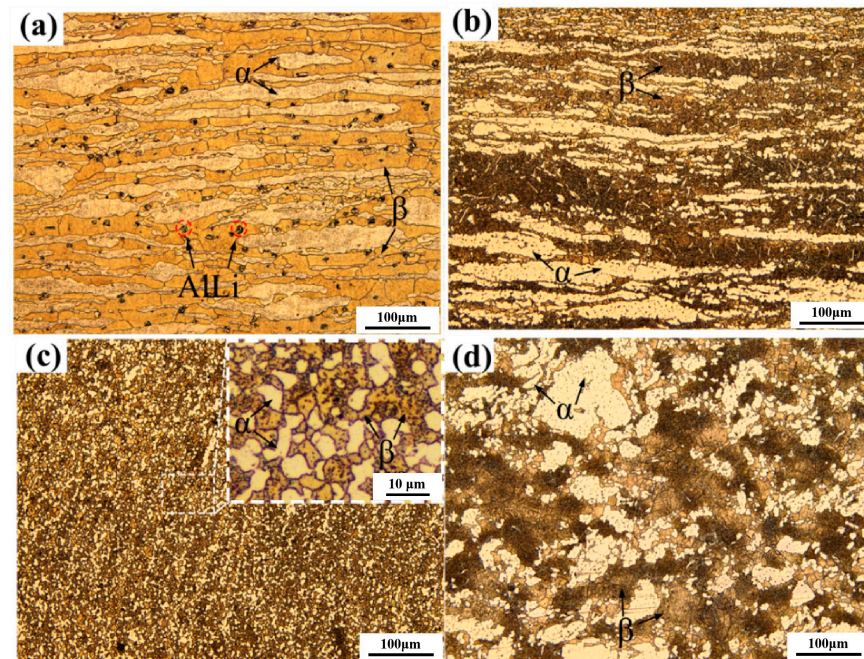

Figure 4. OM images of the (**a**) BM, (**b**) SAZ, and (**c**) FGP in the PAZ and the (**d**) CGP in the PAZ of the joint.

Figures 5–7 show the OM images of the horizontal plane situated 0.5 mm from the top surface of the joints obtained at different welding speeds, which reflects the material flow in the SAZ during the FSW. For all three samples, the pure Mg marker continuously bended around the keyhole, with its thickness first decreasing and subsequently increasing. According to the thickness variation in the pure Mg strip along the flowing trajectory, the whole material flow in the FSW process could be divided into five stages, as denoted in the figures, namely, the preheating stage, the accelerated flow stage, the high-speed flow stage, decelerated flow stage, and the annealing stage [25]. Briefly speaking, in the preheating stage, the material in front of the tool shoulder started to be heated by the frictional heat caused by the tool and had not yet undergone plastic deformation, and the thickness of the pure Mg strip remained unchanged. In the subsequent accelerated flow stage, the materials started to be extruded strongly by the tool and the thickness of the pure Mg strip decreased rapidly. In the high-speed flow stage, the thickness of the Mg strip was minimal and remained largely unchanged, indicating the highest material flow rate at this stage. In the decelerated flow stage, the material flow rate began to be decreased and the thickness of the pure Mg strip became larger due to the accumulation of the materials. The annealing stage was located outside of the SZ, in which the material is subjected to post-weld annealing.
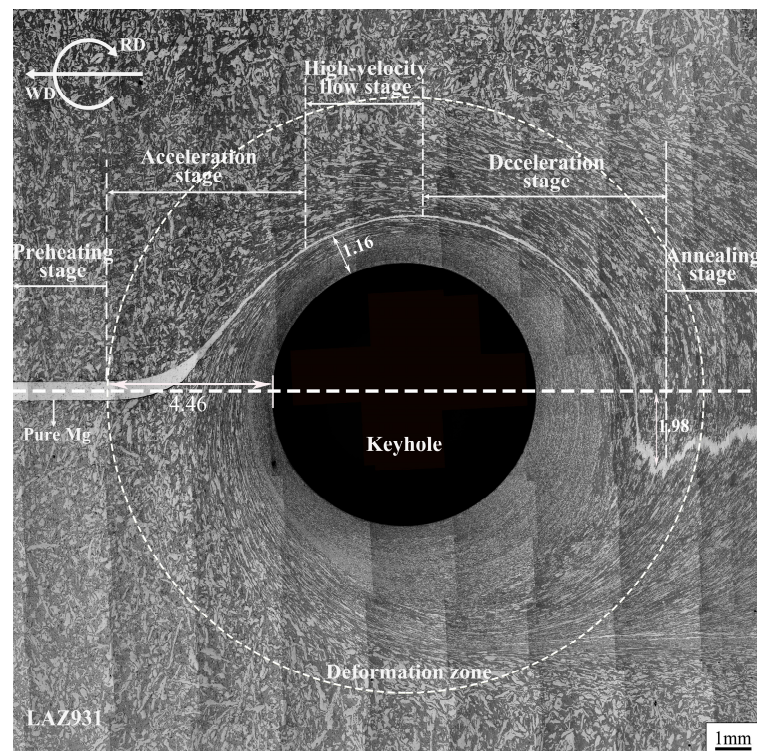
Figure 5. OM macrostructure of the horizontal plane 0.5 mm from the top surface of the joint obtained at a welding speed of 50 mm/min (WD: welding direction; RD: rotation direction).
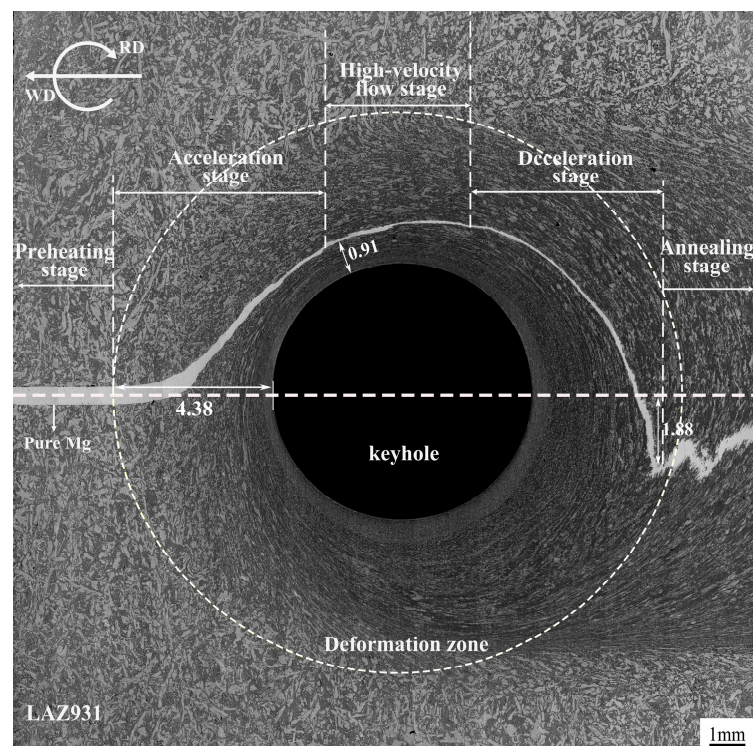
Figure 6. OM macrostructure of the horizontal plane 0.5 mm from the top surface of the joint obtained at a welding speed of 100 mm/min.
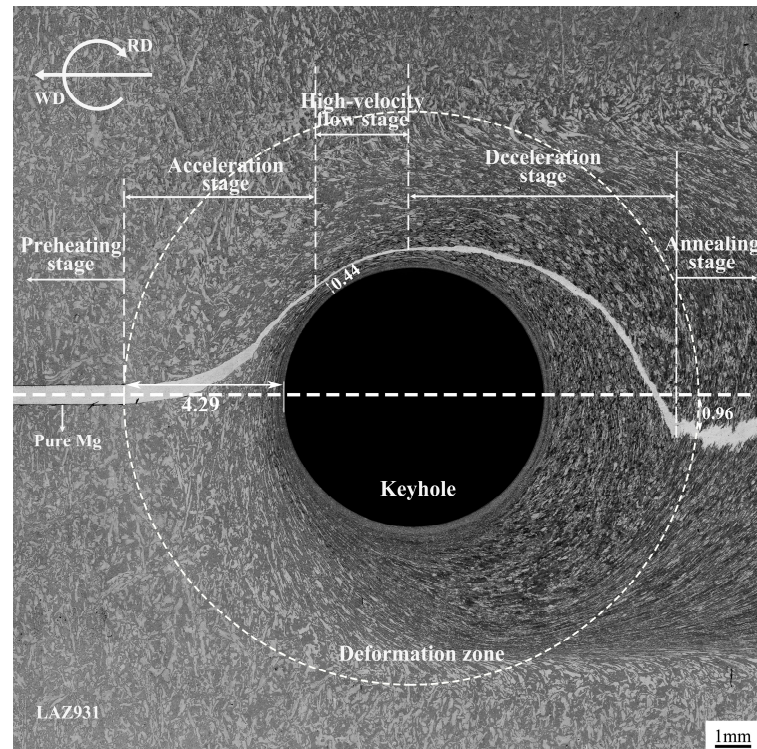
Figure 7. OM macrostructure of the horizontal plane 0.5 mm from the top surface of the joint obtained at a welding speed of 200 mm/min.

In the SAZ, the material flow was primarily driven by shear stress and extrusion from the tool shoulder, which transferred the materials from the AS to the RS. As the welding speed increased, the heat input decreased and the SAZ area shrank, resulting in a reduction in the distance where the pure Mg strip began to deform ahead of the keyhole. Specifically, when the welding speed was increased from 50 to 100 and 200 mm/min, the deformation distance decreased from 4.46 mm to 4.38 mm and 4.29 mm, respectively.

Among these three samples, the minimum distance between the Mg strip and the keyhole was observed in the high-speed flow stage. This distance was approximately 1.16 mm at 50 mm/min, 0.91 mm at 100 mm/min, and 0.44 mm at 200 mm/min, respectively. This indicated that the area of the steady-state flow region reduced as the welding speed increased. The rotating tool deflected the material away from the center of the SZ. The maximum deviation of the deposited Mg strip from the centerline of the joint was 1.98 mm at 50 mm/min, 1.88 mm at 100 mm/min, and 0.96 mm at 200 mm/min, indicating that the capacity of the tool to transfer the materials diminished as the welding speed increased.

According to the above description, the flowing trajectory and thickness variation in the marker material around the keyhole on a horizontal plane 0.5 mm from the top of the joints obtained at different welding speeds was extracted and is shown in Figure 8a, in which a simple coordinate system was established to characterize the material deformation at different locations. The origin of the coordinate system was set at the keyhole center and the positive direction aligned with the opposite welding direction. It can be seen that the material flow behavior of the LAZ931 Mg alloy in the SAZ during the FSW was similar regardless of the welding speeds. Therefore, for the three different welding speeds, the letters "a", "b", "c", "d", and "e" represent the materials located at the preheating stage, accelerating stage, high-speed flowing stage, decelerating stage, and annealing stage during the FSW process, respectively. The point of the smallest thickness on the Mg strip marker was consistently found at position "c", namely, in the high-speed flowing stage. As the welding speed decreased, more material could be plasticized and the Mg strip located further from the tool began to deform due to the increased heat input, leading to a widespread distribution of the marker materials. However, the distance of the Mg strip

from the interface decreased in the deceleration and annealing stages due to the strain reversal [25]. According to Ref. [25], the strain rate at any location × along the flowing trajectory can be calculated based on the thickness variation and the specific welding parameters using the formula shown below:

$$\dot{\varepsilon}_x = \frac{ln\frac{l_{x-0.5}}{l_x}v_il_i(l_{x-0.5}+l_x)}{2d_xl_xl_{x-0.5}}$$

(1)

where l_i and v_i represent the initial thickness of the material and the initial flow velocity, respectively; l_x represents the thickness of the Mg strip at location x and $l_{x-0.5}$ represent the thickness of the Mg strip 0.5 mm ahead of the measured position. The calculated results are shown in Figure 8b. The strain rate increased rapidly when the materials began to be deformed at an accelerated rate and then decreased gradually. The higher the welding speed, the larger the strain rate that was found for the materials. The maximum strain rate could reach about 1.2 in the SAZ when the welding speed was 200 mm/min.
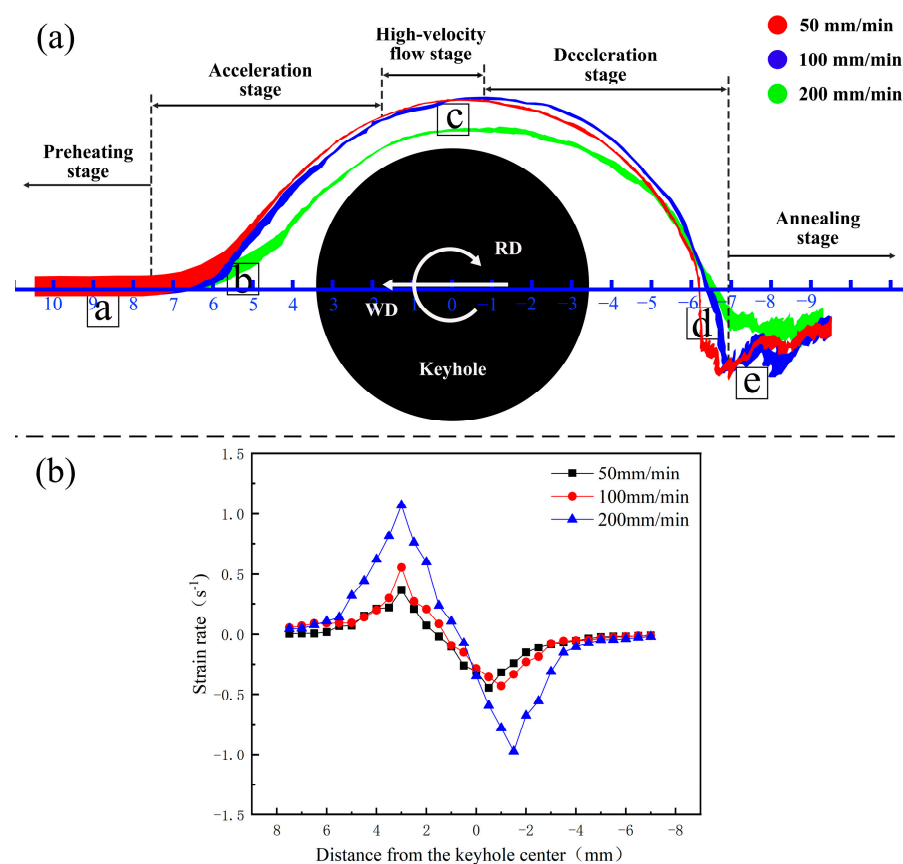

Figure 8. (**a**) Distribution of the marker material and (**b**) distribution of the strain rate around the keyhole in the SAZ of the joints at different welding speeds.

To study the microstructural evolution of the materials in the SAZ, the microstructure of the materials located at positions from "a" to "c" of the joint obtained at 100 mm/min was characterized, as shown in Figure 9. At position "a", the material was merely preheated by the heat emanating from the SZ without undergoing deformation. Consequently, its microstructure remained similar to that of the BM, containing elongated α-Mg and AlLi particles precipitated within the β-Li phases. At position "b", the α-Mg phase began to undergo strong plastic deformation. Compared to the preheating stage, the average grain size of the β-Li phase was significantly refined from 69.5 μm to 30.1 μm. At position "c", the material flow rate reached its maximum value and the overall flow direction of the material was opposite to the welding direction [25]. Part of the α-Mg phase was broken into

smaller particles by the shoulder of the high-speed rotating tool and were dispersed in the elongated β-Li phase. The grain size of the β-Li phase also decreased and the presence of AlLi particles was almost invisible at this stage, which could be attributed to the dissolution of the AlLi phase during the high-temperature plastic deformation. When the material flow reached position "d", the material flow rate and deformation rate slowed down, causing the accumulation of the broken α-Mg small particles. Meanwhile, the grain size of the β-Li phase remained largely unchanged. Finally, at position "e", the materials entered the cooling period after the FSW process was completed. The grain growth of the β-Li phase was suppressed due to the DGG of the α-Mg phase during welding, which effectively pinned the migration of the grain boundaries. The microstructure at position "e" was consistent with that in the SAZ, as shown in Figure 4b.
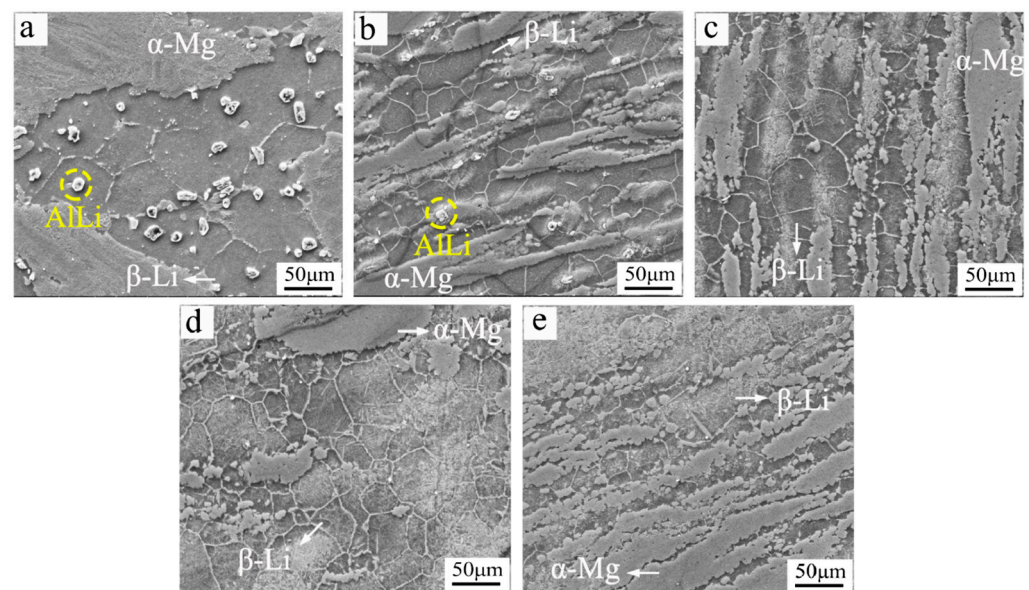
Figure 9. SEM images showing the microstructure of the materials located at different stages during the FSW: (**a**) preheating stage; (**b**) accelerating flow stage; (**c**) high-speed flow stage; (**d**) decelerating stage; (**e**) annealing stage.

Similarly, Figures 10–12 show the OM images of the horizontal plane situated 0.5 mm from the bottom surface of the joints obtained at different welding speeds, which reflected the material flow in the PAZ during the FSW. In the PAZ, the deformation area is smaller than that of the SAZ. Generally, the marker material was discontinuously distributed in the PAZ around the keyhole and, compared with the continuous distribution in the SAZ, it was proposed that the material flow was continuous in the SAZ but discontinuous in the PAZ [26]. In the PAZ, the primary driving force for the material flow is the shearing caused by the pin. As the material flows, it comes in contact with the surface of the pin and transfers sequentially around the pin from the AS to the RS. As a result, the material produced by the shear of the pin is stretched to a periodic, isometric arcuate pattern, known as the "onion ring" pattern.

In Figure 10, the pure Mg marker began to deform at a distance of 1.91 mm in front of the keyhole, which was shorter than the 4.46 mm observed in the SAZ, as shown in Figure 5, while at 100 mm/min and 200 mm/min, this distance was 1.84 mm and 1.34 mm, respectively, as shown in Figures 11 and 12. It was revealed that the area impacted by the pin decreased with the increasing welding speed due to the decreased heat input, similar to the trend observed in the SAZ of the joint. Comparing to the marker material in Figures 10 and 11, the marker material in Figure 12 was bulkier and more clustered due to the increased revolutionary pitch. This also indicates that the material flow became gradually weaker as the welding speed increased.
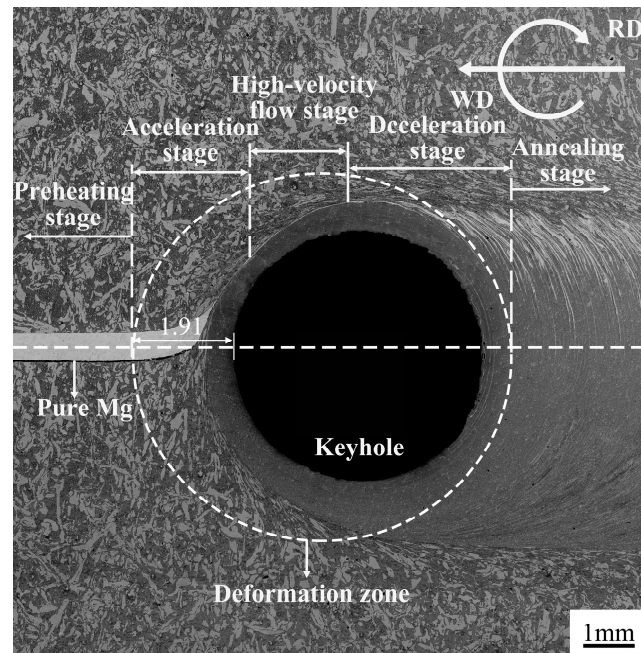
Figure 10. OM microstructure of the horizontal plane 0.5 mm from the bottom of the 50 mm/min joint.
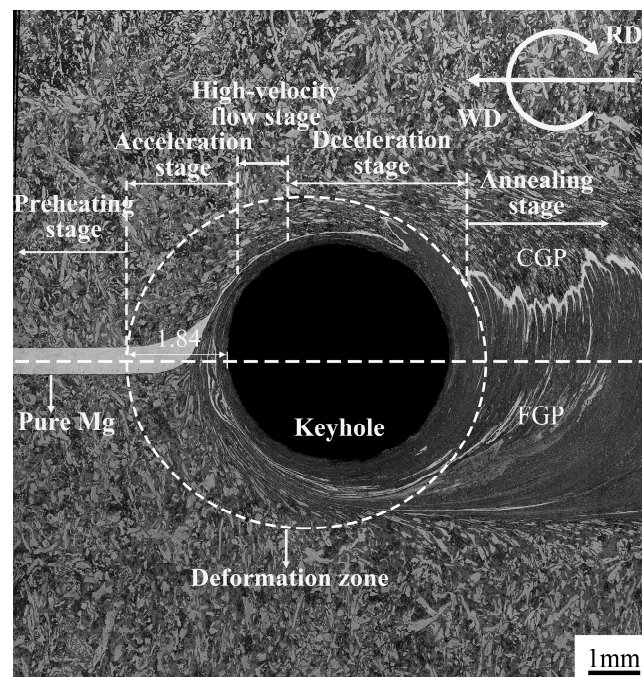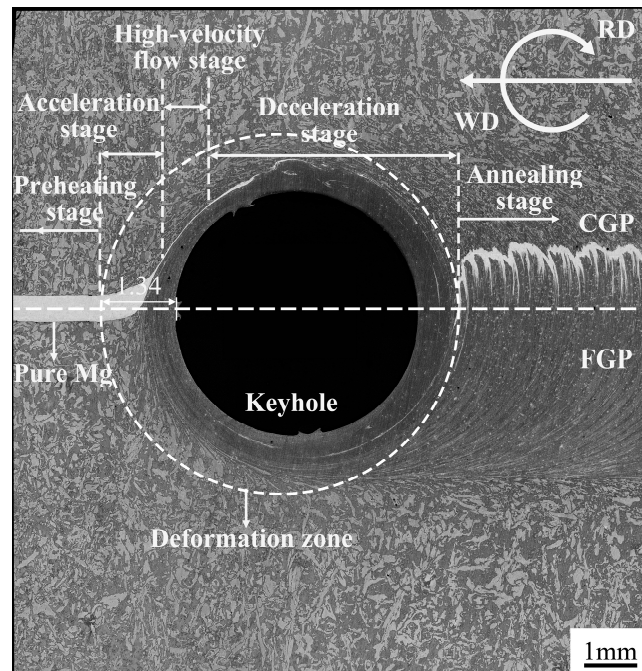

Figure 11. OM microstructure of the horizontal plane 0.5 mm from the bottom of the 100 mm/min joint.

Similar to the microstructure of the PAZ on the cross-sectional plane, as shown in Figure 3, the FGP and CGP divided by the marker material on the horizontal plane of the PAZ were also found to be distributed on the AS and RS within the SZ, respectively. Compared to the SAZ, the width of the pure Mg strip was narrower in the deformation zone, indicating a higher strain rate in the PAZ. As the marking material was continuous in the deformation zone, it indicated that the materials on the AS and RS were generally not mixed with each other during the FSW. However, due to the relatively higher material vertical flowing rate in the PAZ, a slight mixing of the AS and RS behind the rotating tool was casually observed, as shown in Figure 11. It was proposed that, with the pin traveling forward along the interface between the workpiece during the FSW, the material

on the AS came into contact with the pin's surface, was crushed and refined, and was ultimately deposited in the weld to form an FGP. Conversely, the material on the RS did not contact the pin's surface but was directly deposited onto the RS under the pin's impetus, forming a CGP.

Figure 12. OM microstructure of the horizontal plane 0.5 mm from the bottom of the 200 mm/min joint.

Figure 13 shows the flowing trajectory and thickness variation in the marker material around the keyhole on a horizontal plane 0.5 mm from the bottom of the joints obtained at different welding speeds. For all three welding speeds, the flowing behavior of the pure Mg strip was consistent, namely, the thickness of the marker material initially decreased, subsequently increased, and ultimately dispersed within the weld nugget of the joint. As the welding speed increased, the marker material tended to accumulate in the final joint. When the welding speed increased from 50 mm/min to 200 mm/min, the distribution of the marker material began to be coarsened and accumulated into a layer-by-layer pattern, and the distance between the adjacent layer increased due to the increased revolutionary pitch. Similar to that in the SAZ, the strain rate at any location along the flowing trajectory in the PAZ was also calculated, as shown in Figure 13b. The variation in the strain rate was very similar to that in the SAZ. However, the value was significantly larger than that in the PAZ at the same flowing stage. The maximum strain rate could reach about 9.0 in the PAZ when the welding speed was 200 mm/min.

Since the microstructural evolution of the PAZ was similar for joints at different welding speeds, as a typical example, Figure 14 shows the microstructure of the materials at positions from "a" to "e" of the joint at 100 mm/min, as indicated in Figure 13.

At the preheating stage "a", the microstructure remained consistent with that of the BM, which was similar to that at position "a" in the SAZ. At "b" in the accelerated stage, the materials underwent notable deformation, especially on the AS side of the Mg strip closer to the keyhole. Compared with position "b" in the SAZ, as shown in Figure 8, the thickness reduction in the Mg strip at position "b" in the PAZ was significantly larger, indicating the strain rate of the materials was higher in the PAZ [25]. According to the following equation [29]:

$$d^{-1} = a + b \lg Z \tag{2}$$

where *d* is the grain size, *a* and *b* are constant depending on the materials, and *Z* is the Zener–Holloman parameter, described as

$$Z = \dot{\varepsilon}\exp(Q/RT) \tag{3}$$

where $\dot{\varepsilon}$ is the strain rate, *Q* is the activation energy, *R* is the gas constant, and *T* is the temperature; a higher strain rate will lead to a smaller average grain size of the processed materials. According to the calculated strain rate in Figures 8b and 13b, the maximum strain rate was about 9.0 in the PAZ of the 200 mm/min joint, which is much larger than the 1.2 in the SAZ of the 200 mm/min joint. As a result, the microstructure in the SAZ was much coarser than that in the PAZ.
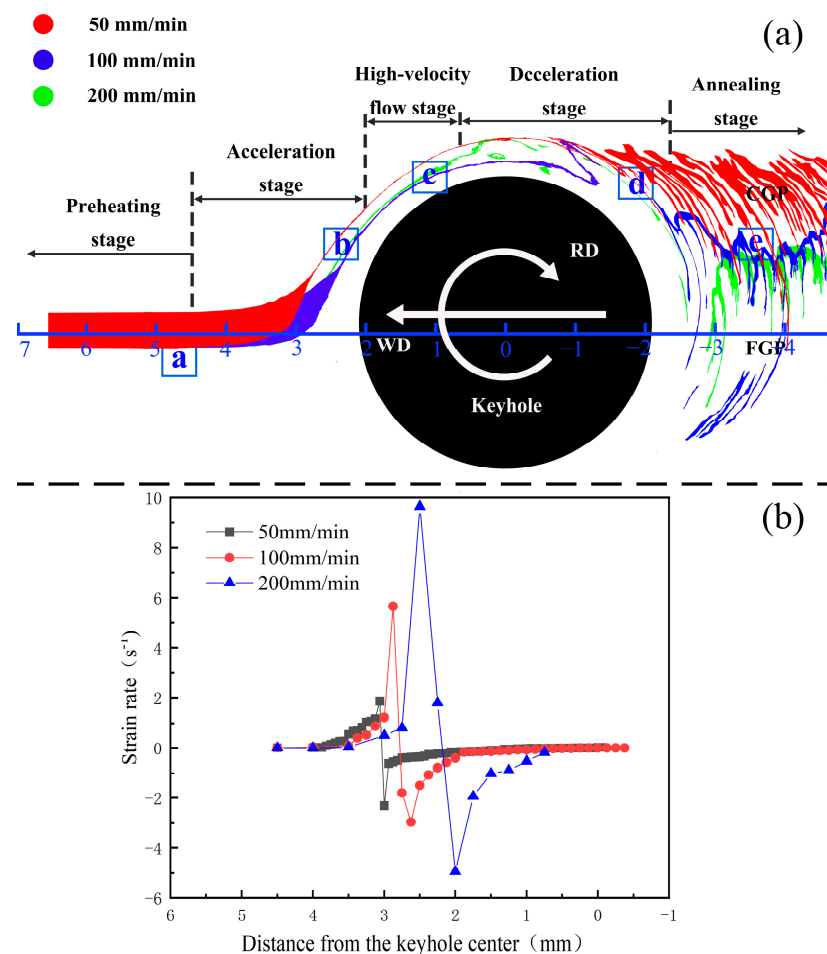
Figure 13. (**a**) Distribution of the marker material and (**b**) distribution of the strain rate around the keyhole in the PAZ of the joints at different welding speeds.

In the PAZ, the α-Mg phase on the AS closer to the pin was elongated and fragmented into small grains, and finally interspersed with the β-Li phase due to the higher strain rate $\dot{\varepsilon}$ of the materials therein. On the outer side of the pure Mg marker away from the keyhole, the α-Mg phase was deformed to a lesser extent at a relatively slower strain rate $\dot{\varepsilon}$, and thus transformed into strip-like aggregates under the driving force of the pin. During the high-speed flowing stage "c", the thickness of the marker material was the smallest, implying that the material flow rate was the highest. The materials between the Mg strip and the keyhole underwent the strongest deformation and further fragmented into uniformly distributed fine particles. On the outer side of the marker material, although the deformation of the elongated α-Mg phase increased further, it still remained as a clustered shape along the flow direction. During the decelerated flow stage "d", the thickness of

the pure Mg strip started to increase, indicating the slowing down of the material flowing rate. The material between the Mg strip and the keyhole experienced continuous severe plastic deformation despite a reduction in the strain rate, ultimately leading to a further refinement of the grain size due to occurrence of DRX, while, on the outer side of the pure Mg marker, the material was further away from the keyhole and deformed at a slower strain rate. Furthermore, because of the DGG effect, the α-Mg was more prone to aggregating together and led to a larger grain size. During the annealing stage "e", the material was no longer deformed and was only subjected to a subsequent cooling period after the FSW. The uniformly dispersed α-Mg phase between the marker material and the keyhole was retained and dispersed with the β-Li phase, which restricted the grain growth of the β-Li phase, forming an FGP on the AS within the SZ. On the outer side of the marker material, the aggregated α-Mg phase and the β-Li phase formed the CGP on the RS within the SZ.
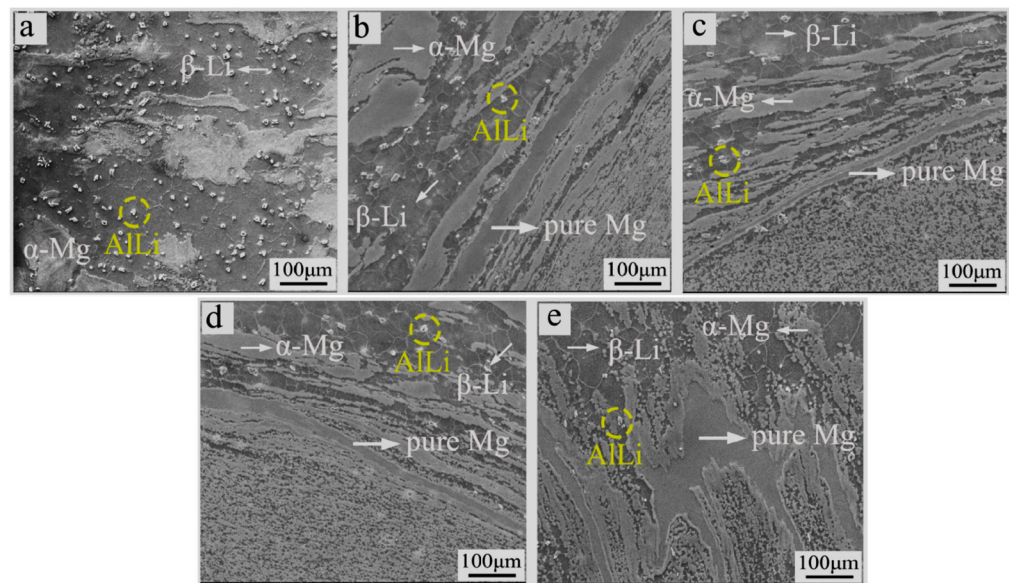
Figure 14. SEM images of the five different stages in the PAZ: (**a**) preheating stage; (**b**) accelerating flow stage; (**c**) high speed flow stage; (**d**) decelerating stage; (**e**) annealing stage.

4. Conclusions

In this study, the material flow and microstructural evolution during the FSW of LAZ931 Mg alloy were investigated using pure Mg strips as the marker materials, and the following conclusions can be drawn:

(1) The material flow of LAZ931 Mg-Li alloy during FSW could divided into the SAZ and the PAZ according to the deformation characteristics of the material. The material flow in both the SAZ and PAZ was weakened with increasing welding speed.

(2) In the SAZ, the marker material was deformed into a strip of uneven thickness, moving closer to the keyhole, and deviating less from the center of the weld by the action of the tool as the welding speed increased; meanwhile, the tool's ability to transfer the material decreased.

(3) In the PAZ, the marker material was dispersed after FSW. With an increasing welding speed, the marked material began to form clusters post-deformation, and the increase in the amount of material transferred by the pin in a single pass resulted in a buildup of material.

(4) The material on the AS was deposited on the AS to form an FGP due to the larger strain-induced DRX, and the material on the RS was deposited on the RS to form a CGP due to the lower strain and DGG effect. As the welding speed increased, there was a noticeable reduction in the volume fraction of the FGP within the SZ.

References

1. Wu, R.; Yan, Y.; Wang, G.; Han, W.; Zhang, Z.; Zhang, M. Recent progress in magnesium–lithium alloys. *Int. Mater. Rev.* **2015**, *60*, 65–100. [CrossRef]
2. Wu, L.; Cui, C.; Wu, R.; Li, J.; Zhan, H.; Zhang, M. Effects of Ce-rich RE additions and heat treatment on the microstructure and tensile properties of Mg–Li–Al–Zn-based alloy. *Mater. Sci. Eng. A* **2011**, *528*, 2174–2179. [CrossRef]
3. Atkins, G.; Marya, M.; Olson, D.; Eliezer, D. Magnesium-lithium alloy weldability: A microstructural characterization. *JOM* **2004**, *6*, 37–41.
4. Fu, J.; Wang, Z.; Liu, W.; Yuan, J.; Jia, C.; Yang, L. Effects of heat input on microstructures and mechanical properties of LAZ931 magnesium-lithium alloy by CO_2 laser welding. *Mater. Today Commun.* **2023**, *35*, 105536. [CrossRef]
5. Ning, J.; Zhang, L.-J.; Han C-q Zhang, H.-B.; Lei, X.-W.; Han, B.-F. Fiber laser welding characteristics of the butt welded joint of novel ultralight Mg-10.1Li-3.1Al-2.9Zn alloy. *Mater. Res. Express* **2019**, *6*, 106545. [CrossRef]
6. Singh, K.; Singh, G.; Singh, H. Review on friction stir welding of magnesium alloys. *J. Magnes. Alloy* **2018**, *6*, 399–416. [CrossRef]
7. Cao, F.R.; Ding, H.; Li, Y.L.; Zhou, G.; Cui, J.Z. Superplasticity, dynamic grain growth and deformation mechanism in ultra-light two-phase magnesium–lithium alloys. *Mater. Sci. Eng. A* **2010**, *527*, 2335–2341. [CrossRef]
8. Padhy, G.K.; Wu, C.S.; Gao, S. Friction stir based welding and processing technologies—Processes, parameters, microstructures and applications: A review. *JMST* **2018**, *34*, 1–38. [CrossRef]
9. Mishra, R.S.; Ma, Z.Y. Friction stir welding and processing. *Mat. Sci. Eng. R.* **2005**, *50*, 1–78. [CrossRef]
10. Threadgill, P.L.; Leonard, A.J.; Shercliff, H.R.; Withers, P.J. Friction stir welding of aluminium alloys. *Int. Mater. Rev.* **2013**, *54*, 49–93. [CrossRef]
11. Xu, N.; Qiu, Z.; Ren, Z.; Wang, D.; Shen, J.; Song, Q.; Zhao, J.; Bao, Y. Microstructure and mechanical properties of friction stir welded ultralight Mg-14Li-1Al alloy. *Mater. Charact.* **2022**, *194*, 112463. [CrossRef]
12. Liu, G.; Ma, Z.; Wei, G.; Xu, T.; Zhang, X.; Yang, Y.; Xie, W.; Peng, X. Microstructure tensile properties corrosion behavior of friction stir processed Mg-9Li-1Zn alloy. *J. Mater. Process. Technol.* **2019**, *267*, 393–402. [CrossRef]
13. Tsujikawa, M.; Abe, Y.; Oki, S.; Higashi, K.; Hiraki, I.; Kamita, M. Cold-rolled Mg-14 mass% Li-1 mass% Al alloy and its friction stir welding. *Mater. Trans.* **2006**, *47*, 1077–1081. [CrossRef]
14. Zhou, M.; Morisada, Y.; Fujii, H.; Wang, J.-Y. Microstructure and mechanical properties of friction stir welded duplex Mg–Li alloy LZ91. *Mater. Sci. Eng. A* **2020**, *773*, 138730. [CrossRef]
15. Gao, S.; Zhao, H.; Li, G.; Ma, L.; Zhou, L.; Zeng, R.; Li, D. Microstructure properties natural ageing behavior of friction stir welded dual-phase Mg-Li alloy. *J. Mater. Process. Technol.* **2024**, *324*, 118252. [CrossRef]
16. Zhou, M.; Zeng, Z.; Cheng, C.; Morisada, Y.; Shi, Q.; Wang, J.-Y.; Fujii, H. Effect of the processing route on the microstructure mechanical behavior of superlight Mg-9Li-1Zn alloy via friction stir processing. *J. Magnes. Alloy* **2022**, *10*, 3064–3081. [CrossRef]
17. Fonda, R.W.; Rowenhorst, D.J.; Knipling, K.E. 3D Material Flow in Friction Stir Welds. *Metall. Mater. Trans. A* **2018**, *50*, 655–663. [CrossRef]
18. Liu, F.C.; Feng, A.H.; Pei, X.; Hovanski, Y.; Mishra, R.S.; Ma, Z.Y. Friction stir based welding, processing, extrusion and additive manufacturing. *Prog. Mater. Sci.* **2024**, *146*, 101330. [CrossRef]
19. Dialami, N.; Cervera, M.; Chiumenti, M. Defect formation and material flow in Friction Stir Welding. *Eur. J. Mech.—A/Solids* **2020**, *80*, 103912. [CrossRef]
20. Dialami, N.; Chiumenti, M.; Cervera, M.; Agelet de Saracibar, C.; Ponthot, J.P. Material flow visualization in Friction Stir Welding via particle tracing. *Int. J. Mater. Form.* **2013**, *8*, 167–181. [CrossRef]
21. Li, W.Y.; Li, J.F.; Zhang, Z.H.; Gao, D.L.; Chao, Y.J. Metal Flow during Friction Stir Welding of 7075-T651 Aluminum Alloy. *Exp. Mech* **2013**, *53*, 1573–1582. [CrossRef]
22. Morisada, Y.; Imaizumi, T.; Fujii, H.; Matsushita, M.; Ikeda, R. Three-Dimensional Visualization of Material Flow During Friction Stir Welding of Steel and Aluminum. *J. Mater. Eng. Perform.* **2014**, *23*, 4143–4147. [CrossRef]
23. de Leon, M.; Shin, H.S. Material flow behaviours during friction stir spot welding of lightweight alloys using pin and pinless tools. *Sci. Technol. Weld. Join.* **2016**, *21*, 140–146. [CrossRef]

24. Zhang, H.; Wu, H.; Huang, J.; Lin, S.; Wu, L. Effect of welding speed on the material flow patterns in friction stir welding of AZ31 magnesium alloy. *Rare Met.* **2007**, *26*, 158–162. [CrossRef]

25. Liu, X.C.; Sun, Y.F.; Nagira, T.; Ushioda, K.; Fujii, H. Experimental evaluation of strain and strain rate during rapid cooling friction stir welding of pure copper. *Sci. Technol. Weld. Join.* **2019**, *24*, 352–359. [CrossRef]

26. Liu, X.C.; Wu, C.S. Material flow in ultrasonic vibration enhanced friction stir welding. *J. Mater. Process. Technol.* **2015**, *225*, 32–44. [CrossRef]

27. Zhang, Q.; Xie, H.; Huang, L.; Wang, L.; Sun, Y.; Guan, S. Microstructure and Mechanical Properties of Friction Stir Welded LAZ931 Duplex Mg-Li Alloy Plates. *J. Mater. Eng. Perform.* 2023, *in press*. [CrossRef]

28. Liu, X.; Wu, C.; Padhy, G.K. Characterization of plastic deformation and material flow in ultrasonic vibration enhanced friction stir welding. *Scr. Mater.* **2015**, *102*, 95–98. [CrossRef]

29. Chang, C.I.; Lee, C.J.; Huang, J.C. Relationship between grain size and Zener–Holloman parameter during friction stir processing in AZ31 Mg alloys. *Scr. Mater.* **2004**, *51*, 509–514. [CrossRef]